Research Article | Vol. 33, No. 22 / 3 Nov 2025 / Optics Express 46313
Optics EXPRESS

Generalized Van Cittert-Zernike Schell propagator: an efficient algorithm for simulating partially coherent light

MANUEL MONTOYA,[1,2,*] MARIA J. LOPERA,[3,4] YUNFENG NIE,[3] AND DAVID BLINDER[1,2]

[1]Department of Electronics and Informatics (ETRO), Vrije Universiteit Brussel (VUB), Pleinlaan 2, B-1050 Brussel, Belgium
[2]IMEC, Kapeldreef 75, B-3001 Leuven, Belgium
[3]Brussels Photonics Team, Department of Applied Physics and Photonics, Vrije Universiteit Brussel (VUB), Pleinlaan 2, B- 1050 Brussels, Belgium
[4]Optics and Photonics Laboratory, School of Applied Sciences and Engineering, Universidad EAFIT, Medellín, Colombia
*manuel.montoya.zuluaga@vub.be

Abstract: We present a wave propagation algorithm that models the diffraction of partially spatially coherent light and can be efficiently computed using a single forward propagation. The model uses the Van Cittert-Zernike theorem to find the complex coherence factor from a light source reaching the object plane, and it then uses the generalized Schell's theorem to compute the diffraction pattern produced at a given propagation distance, not limited to the far field. The numerical propagation is computed by a series of fast Fourier transforms, and it can be adapted to use any existing coherent propagator, giving it high flexibility with minimal additional computational cost. We report speed improvements up to two orders of magnitude and accuracy improvements up to three orders of magnitude over sample-based methods to model partially spatially coherent light in computer-generated holography (CGH) and digital holography (DH).

1. Introduction

Diffraction algorithms that model the propagation of coherent light waves, such as the angular spectrum method, Fresnel diffraction, or Fraunhofer diffraction, are well-established techniques in optics and photonics [1,2]. They are used in many applications in science and engineering, including astronomy, telecommunications, antenna systems, medical imaging, digital holography (DH), and computer-generated holography (CGH), among many others [3–8]. Several efficient implementations of these methods exist in the literature, and most of them are based on the Fast Fourier Transform (FFT) [9]. However, as these models assume perfect temporal and spatial coherence, their applicability in real-world scenarios is often limited to highly coherent light sources such as lasers.

In recent years, a lot of research has been focused on modeling the propagation of partially coherent light sources, which involves more complicated and computationally demanding algorithms than those required in the coherent case. This study focuses specifically on spatial coherence. The propagation in this case can be modeled using the Wigner function, which is a four-dimensional (4D) representation composed of two spatial and two angular dimensions, also referred to as phase-space [10,11]. Recently, a phase-space propagator was proposed leveraging the shear transformation property of the phase-space density function [12]; nevertheless, it still requires large memory and computation resources in practice, especially in the case of two-dimensional (2D) propagation. A different approach is the coherent mode expansion (CME), where the spatial coherence properties of the light are represented as the superposition

#571673 https://doi.org/10.1364/OE.571673
Journal © 2025 Received 1 Jul 2025; revised 27 Aug 2025; accepted 14 Oct 2025; published 23 Oct 2025

Optics EXPRESS

of independent coherent modes, and each mode is propagated independently using coherent propagation [13]. This method has been widely used in optical communication research for modeling the propagation of partially coherent beams in atmospheric turbulence [14]. With the CME method, the 4D problem is broken down into a set of 2D problems, often making it more approachable from a computational viewpoint; however, the number of modes that have to be propagated is not small in general, still making it impractical for many applications. A similar way of modeling partial coherence was proposed by Vahimaa and Turunen [15]. The idea is to represent the light source as a collection of finite point sources and then use coherent propagation for each source, integrating the results incoherently at the camera plane. This technique is valid for quasihomogeneous sources, such as LEDs, and it has been used in a wide range of applications, including DH and CGH [16,17]. Again, the main drawback of this model is that it requires a number M of propagations that is given by the number of samples from the light source, which increases along with its size, making it inefficient for simulations involving lower spatial coherence. To improve the computational efficiency of this method, Horisaki et al. recently proposed an approximation denominated compressive propagation (CP), and successfully applied it to CGH, achieving promising results in a low-cost color 3D display system [18–20]. The authors presented two different approximations, one involving planar wavefronts (CP-P) and one involving random wavefronts (CP-R). In CP-P, a random subset of M point sources from the light source is propagated as plane waves, whereas in CP-R, M random wavefronts are generated and propagated. In their experiments, the authors used $M = 30$, requiring the calculation of 30 forward coherent propagations in each iteration of the CGH optimization process. CP-R showed better results, and hence it was the chosen method in the latest studies.

Even though compressive propagation improves over the previous works in CGH in terms of computational efficiency, it still suffers from a major drawback: the trade-off between diffraction accuracy and the number M of coherent propagations. As this number is lowered to reach lower computation times, the accuracy of the partially coherent model decreases. In this work, we explore a significantly different approach for modeling partially spatially coherent light, which is based on the Van Cittert-Zernike and the generalized Schell's theorems [2,21]; and show its enormous potential for CGH, DH [22], and computational imaging in general. The Van Cittert-Zernike theorem describes how the mutual intensity propagates away from an incoherent source, and it can be computed numerically by simply taking the FFT of the intensity distribution. On the other hand, the generalized Schell's theorem provides a general way of calculating diffraction patterns generated by partially coherent illumination of an aperture, removing the far field restriction that is present in the widely known Schell's theorem [23]. This theorem can also be efficiently implemented using multiple FFTs; hence, the final algorithm only requires one forward propagation and only uses the Fresnel and paraxial approximations. In spite of its great potential, the generalized Schell's theorem has not been applied in many fields where it could represent an invaluable contribution. To the best of the authors' knowledge, only a few works have implemented this theorem numerically so far, some notable examples being the works by Waller et al. in quantitative phase imaging [24], by Liu et al. in holographic display systems [25], and by Wang et al. for modeling beam propagation in random media [26,27]. Here we propose the Generalized Van Cittert-Zernike Schell propagator (GVS): a novel algorithm that integrates the Van Cittert-Zernike theorem with the generalized Schell's theorem to model the propagation of partially spatially coherent light. In [27], the authors employ a convolution-based approach analogous to the generalized Schell's theorem, to find the propagated intensity produced by a Schell model source. In [25], the authors derive an efficient algorithm using the Van Cittert-Zernike and generalized Schell's theorems, with the analytical solution of the Van Cittert-Zernike theorem for the special case of a circular source. The main difference in our proposal is that, instead of starting with a given coherence function (Ref. [27]) or calculating it analytically for a special case (Ref. [25]), we derive the complete numerical solution that

Optics EXPRESS

integrates both theorems, enabling the diffraction calculation for incoherent light sources of arbitrary intensity distributions.

The implementation of the proposed algorithm has some practical implications, which are comparable to those of the coherent Fresnel diffraction. The derivation of the algorithm relies on the paraxial approximation [2], which restricts the minimum propagation distance that can be used for the model to yield correct results. Also, zero-padding should be used to avoid aliasing effects produced by circular convolution, as is done in [9]. Moreover, the sampling requirements to avoid aliasing effects from the quadratic phase factors (chirp functions) are also inherited from the coherent propagation for the case of spherical illumination with a propagation distance from the source plane to the object plane. A detailed study of these requirements is presented in [28]. Finally, the Fourier transforms used by the proposed algorithm have different scales between input and output planes. This scaling must be taken into account to ensure proper results, as is explained in section 3.

In this work, through a series of numerical simulations and experimental validations, we demonstrate that the proposed partially coherent algorithm is highly accurate, and it is several orders of magnitude faster than other methods currently used in CGH and DH. Furthermore, we show that the proposed model can be adapted to use any existing coherent propagator, giving it great flexibility and making it a strong candidate for CGH and DH applications in the future.

2. Propagation of partially coherent light

The general expression for the propagation of mutual intensity, with the geometry shown in Fig. 1(a), and assuming quasimonochromatic illumination, is given by Eq. (1) [2],

$$J(Q_1, Q_2) = \iiiint_{\Sigma} J(P_1, P_2) e^{-ik(r_2 - r_1)} \frac{\chi(\theta_1)}{\lambda r_1} \frac{\chi(\theta_2)}{\lambda r_2} dS_1 dS_2, \tag{1}$$

where Q_k are points in the output plane, J is the mutual intensity function, P_k are points in the input plane, r_k are the distances between Q_k and P_k, θ_k are the angles between r_k and the normal to the surface Σ at P_k, χ is an obliquity factor, $k = 2\pi/\lambda$ is the wavenumber, with λ the wavelength of the light source, i is the imaginary unit, and S_k are two different integrations over the same surface Σ. We start with the assumption of a perfectly incoherent light source described by a mutual intensity of the form $J(u_1, v_1; u_2, v_2) = \kappa I(u_1, v_1)\delta(u_1 - u_2, v_1 - v_2)$, where δ denotes the Dirac delta function [2]. By using the paraxial approximation and the geometry presented in Fig. 1(b), we get the final form of the Van Cittert-Zernike theorem [2],

$$J(\xi_1, \eta_1; \xi_2, \eta_2) = \frac{\kappa e^{-i\psi}}{(\lambda z_{so})^2} \iint_{-\infty}^{\infty} I(u, v) e^{i\frac{k}{z_{so}}(u\Delta\xi + v\Delta\eta)} du dv, \tag{2}$$

where z_{so} is the distance between the source and object planes, (ξ, η) are the spatial dimensions in the object plane, (u, v) in the source plane, I is the intensity distribution of the source, $\Delta\xi = \xi_2 - \xi_1$, $\Delta\eta = \eta_2 - \eta_1$, $\kappa = \lambda^2/\pi$ for an incoherent source and the phase factor $\psi = \frac{\pi}{\lambda z_{so}}\left[(\xi_2^2 + \eta_2^2) - (\xi_1^2 + \eta_1^2)\right]$. Now, noting that the integral term corresponds to the Fourier transform of I (scaled by the factor $1/\lambda z_{so}$), we can use the normalized version of Eq. (2) to express the complex coherence factor μ (also referred to as complex degree of coherence) in terms of the phase factor ψ and the quantity $\mu_{\mathcal{F}}$, which we find by normalizing the Fourier transform of the source intensity distribution [2],

$$J = I_0 \mu\left(\frac{\xi_1}{\lambda z_{so}}, \frac{\eta_1}{\lambda z_{so}}; \frac{\xi_2}{\lambda z_{so}}, \frac{\eta_2}{\lambda z_{so}}\right) = I_0 e^{-i\psi} \mu_{\mathcal{F}}\left(\frac{\Delta\xi}{\lambda z_{so}}, \frac{\Delta\eta}{\lambda z_{so}}\right), \tag{3}$$

$$\mu_{\mathcal{F}}\left(\frac{\Delta\xi}{\lambda z_{so}}, \frac{\Delta\eta}{\lambda z_{so}}\right) = \frac{\boldsymbol{F}\{I(u, v)\}}{|\boldsymbol{F}\{I(u, v)\}|_{\mathrm{MAX}}}, \tag{4}$$

Optics EXPRESS

where $I_0 = \kappa/(\lambda z_{so})^2$, $|\cdot|_{\mathrm{MAX}}$ denotes the maximum absolute value, and $\boldsymbol{F}\{\cdot\}$ denotes the 2D Fourier transform operator. We note that $\mu_{\mathcal{F}}$ is a 2D function that only depends on $\Delta\xi$ and $\Delta\eta$, and the pixel pitch in the object plane changes in proportion to $1/\lambda z_{so}$.

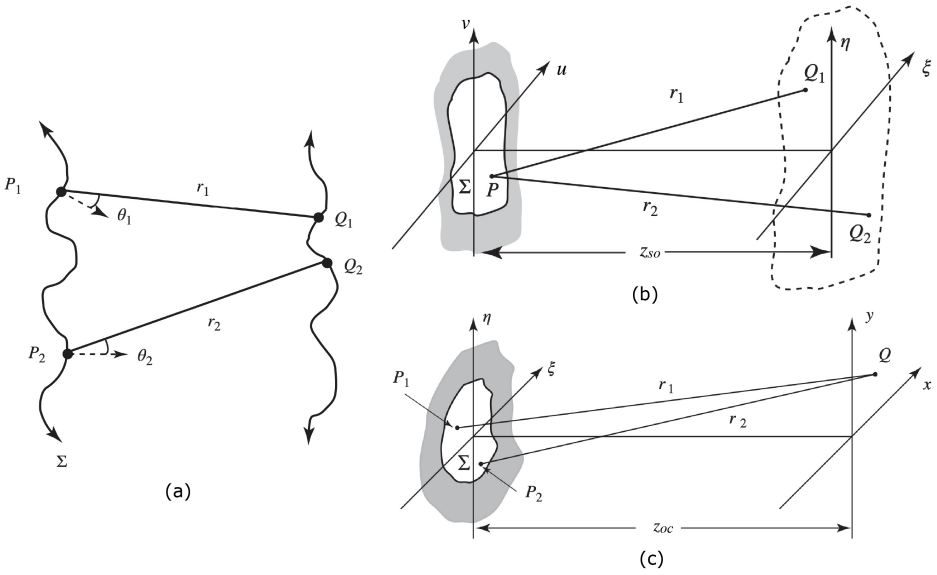

Fig. 1. Geometries for the propagation of partially coherent light (adapted with permission from [2], §5 Figs. 5.21, 5.22 and 5.24); (a) Propagation of mutual intensity; (b) Van Cittert-Zernike theorem; (c) Generalized Schell's theorem.

Subsequently, we use the propagation of mutual intensity once more to find the intensity reaching the camera plane $I(x, y)$ after the interaction of light with the object plane $P(\xi, \eta)$, using the geometry shown in Fig. 1(c). Substituting Eq. (3) in Eq. (1) and assuming a thin transmitting structure in the object plane, we obtain Eq. (5), where we have chosen the cosine function as obliquity factor [2],

$$I(x,y) = \frac{I_0}{\lambda^2} \iiiint_{-\infty}^{\infty} P(\xi_1,\eta_1)P^*(\xi_2,\eta_2)\mu_{\mathcal{F}}(\xi_2-\xi_1,\eta_2-\eta_1) \\ e^{-i\psi}e^{-ik(r_2-r_1)}\frac{\cos(\theta_1)}{r_1}\frac{\cos(\theta_2)}{r_2}d\xi_1 d\eta_1 d\xi_2 d\eta_2. \tag{5}$$

We then use the paraxial and Fresnel approximations to write Eq. (6) in terms of quadratic phase factors [2],

$$I(x,y) = \frac{I_0}{(\lambda z_{oc})^2} \iiiint_{-\infty}^{\infty} P(\xi_1,\eta_1)P^*(\xi_2,\eta_2)\mu_{\mathcal{F}}(\xi_2-\xi_1,\eta_2-\eta_1) \\ e^{-i\frac{k}{2z_{so}}[(\xi_2^2+\eta_2^2)-(\xi_1^2+\eta_1^2)]}e^{i\frac{k}{2z_{oc}}[(x-\xi_1)^2+(y-\eta_1)^2]}e^{-i\frac{k}{2z_{oc}}[(x-\xi_2)^2+(y-\eta_2)^2]}d\xi_1 d\eta_1 d\xi_2 d\eta_2, \tag{6}$$

where z_{oc} is the distance between the object and camera planes. We emphasize now that the phase factor ψ coming from the Van Cittert-Zernike theorem can be operated in this step with the quadratic phase factors of the object plane obtained in Eq. (6). This enables the integration of the two theorems into a single efficient propagation algorithm. By letting $\Delta\xi = \xi_2 - \xi_1$, $\Delta\eta = \eta_2 - \eta_1$,

Optics EXPRESS

$\delta = \frac{1}{z_{so}} + \frac{1}{z_{oc}}$, and reordering the terms of the equation, we can write

$$I(x,y) = \frac{I_0}{(\lambda z_{oc})^2} \iint_{-\infty}^{\infty} \mu_{\mathcal{F}}(\Delta\xi,\Delta\eta) e^{-i\frac{k\delta}{2}(\Delta\xi^2+\Delta\eta^2)} e^{-i\frac{k}{z_{oc}}(x\Delta\xi+y\Delta\eta)} \left[\iint_{-\infty}^{\infty} P(\xi_1,\eta_1) P^*(\xi_1-\Delta\xi,\eta_1-\Delta\eta) e^{ik\delta(\xi_1\Delta\xi+\eta_1\Delta\eta)} d\xi_1 d\eta_1 \right] d\Delta\xi d\Delta\eta. \tag{7}$$

Similar to the derivation of the generalized Schell's theorem [21], we can define $P'(\xi_1,\eta_1) = P(\xi_1,\eta_1)e^{i\frac{k\delta}{2}(\xi_1^2+\eta_1^2)}$ to write the propagation as the Fourier transform of the product of two functions, where $\mathcal{P}'$ is the autocorrelation of P',

$$I(x,y) = \frac{I_0}{(\lambda z_{oc})^2} \iint_{-\infty}^{\infty} \mathcal{P}'(\Delta\xi,\Delta\eta) \mu_{\mathcal{F}}(\Delta\xi,\Delta\eta) e^{-i\frac{k}{z_{oc}}(x\Delta\xi+y\Delta\eta)} d\Delta\xi d\Delta\eta, \tag{8}$$

$$\mathcal{P}'(\Delta\xi,\Delta\eta) = \iint_{-\infty}^{\infty} P'(\xi_1,\eta_1) P'^*(\xi_1-\Delta\xi,\eta_1-\Delta\eta) d\xi_1 d\eta_1. \tag{9}$$

It is important to note here that we have just transformed our previous 4D problem into a 2D problem that can be computed efficiently. The numerical propagation in terms of operators is then given by Eq. (10), where $\boldsymbol{F^{-1}}\{\cdot\}$ denotes the 2D inverse Fourier transform operator, and it is critical to ensure the consistency in the dimensions of $\mu_{\mathcal{F}}$ and the autocorrelation of P'.

$$I\left(\frac{x}{\lambda z_{oc}}, \frac{y}{\lambda z_{oc}}\right) = \frac{I_0}{(\lambda z_{oc})^2} \boldsymbol{F}\left\{ \boldsymbol{F^{-1}}\left\{ \left\| \boldsymbol{F}\left\{ P(\xi,\eta) e^{i\frac{k\delta}{2}(\xi^2+\eta^2)} \right\} \right\|^2 \right\} \mu_{\mathcal{F}}(\Delta\xi,\Delta\eta) \right\}. \tag{10}$$

Finally, we note that the term inside the autocorrelation corresponds to the intensity of the coherent propagation of the object multiplied by the quadratic phase factor from the Van Cittert-Zernike theorem, $P(\xi,\eta)e^{i\frac{k}{2z_{so}}(\xi^2+\eta^2)}$. This enables the use of any coherent propagation method to compute the propagation of mutual intensity:

$$I(x,y) = \frac{I_0}{(\lambda z_{oc})^2} \boldsymbol{F}\left\{ \boldsymbol{F^{-1}}\left\{ I_{\text{coherent}} \right\} \mu_{\mathcal{F}}(\Delta\xi,\Delta\eta) \right\}. \tag{11}$$

3. Numerical simulations

We implemented GVS using Python. An open-source repository containing the implementation and examples can be found online [29]. Figure 2 shows the numerical setup for the simulations, where we use discrete square grids of $N \times N$ pixels, and we perform zero-padding in the spatial domain to avoid aliasing issues. To account for the pixel pitch variation between the input and output planes in Eqs. (3) and (10), we fixed the camera pixel pitch (Δx_c) and computed the required pixel pitches in the object (Δx_o) and source planes (Δx_s) according to Eq. (12).

$$\Delta x_o = \frac{\lambda z_{oc}}{2\Delta x_c N}, \qquad \Delta x_s = \frac{\lambda z_{so}}{2\Delta x_o N} \tag{12}$$

For validation, we simulated the standard double pinhole experiment under different conditions and implemented multiple models for comparison. We present the description and properties of each model in Table 1. Under the I_{coherent} GVS model, we implemented three different variations: Shifted Fresnel GVS (SF-GVS), Fresnel Convolution GVS (FC-GVS), and Angular Spectrum GVS (AS-GVS).

Figure 3(a) shows the diffraction patterns obtained by the GVS model and the far field Schell model as a function of the source radius (r_s), clearly illustrating the limitation of the latter for short distance calculation; r_p and Δ_p correspond to the pinhole radius and the distance between the center of the pinholes, respectively. In Fig. 3(b), we compare the central cross-section along

Optics EXPRESS

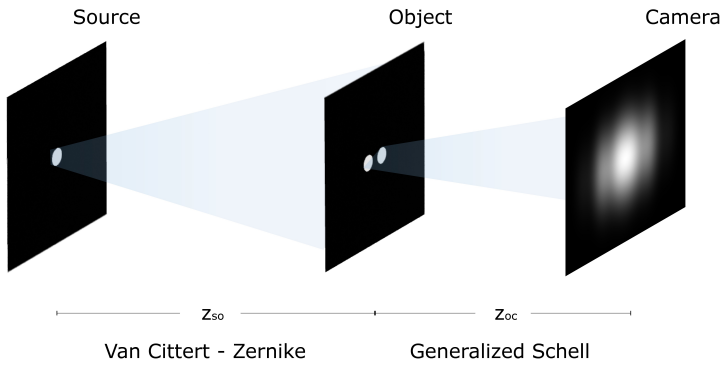

Fig. 2. Scheme of the geometrical setup used for the simulations. The source intensity distribution is represented as a uniform white circle with variable radius, and it is propagated a distance z_{so} from the source plane to the object plane to find $\mu_{\mathcal{F}}$ by using the Van Cittert-Zernike theorem, cf. Equation (4). The generalized Schell's theorem is then applied to find the diffracted intensity reaching the camera plane at z_{oc}, cf. Equations (10) and (11).

Table 1. Partially Coherent Propagation Models

Model	Description	Computational Complexity	Pixel Pitch	Off-axis calculation
Integral Computation	Discretized version of Eq. (5); $\mu_{\mathcal{F}}$ is computed using Eq. (3).	$O(N^6)$	Arbitrary	Yes
GVS	Eq. (10).	$O(N^2 \log N)$	Restricted	No
I_{coherent} GVS	Eq. (11), using the I_{coherent} implementations described in [9].	$O(N^2 \log N)$	Arbitrary	Yes
Finite Point Sources	Coherent propagation from all the point sources (M_s). Sum of intensities in the camera plane [15–17].	$O(M_s\, N^2 \log N)$	Arbitrary	Yes
CP-R	Coherent propagation of M random wavefronts. Sum of intensities in the camera plane [18–20].	$O(M\, N^2 \log N)$	Arbitrary	Yes
Schell (Far field)	Far field Schell's theorem [23].	$O(N^2 \log N)$	Restricted	No

the x axis obtained with the different models. Our reference models are integral computation 1 and 2, which are the full 4D numerical integral evaluation of GVS in Eq. (5). For the integral computation 1, the GVS and the SF-GVS models we set Δx_o and Δx_s corresponding to Eq. (12), while for the remaining models we set $\Delta x_o = \Delta x_c$ and keep Δx_s as in Eq. (12). The reason behind this difference in the calculation is that in GVS, the pixel pitch changes between the object and camera planes, while in the AS-GVS and the FC-GVS models, the pixel pitch remains constant; therefore, we calculated the integral computation 2 to have a fair comparison with the constant pixel pitch models. For the coherent propagation in the finite point sources and CP-R methods, we used the angular spectrum. The results from the different models show excellent agreement. The biggest differences arise in the CP-R models (indicated by black arrows), evidencing the trade-off between computational efficiency and accuracy for this type of model. For the case of $r_s = 1000\ \mu m$, the mean-squared-error (MSE) was 2.7×10^{-2} for CP-R ($M = 30$), and 2.6×10^{-2} for CP-R ($M = 300$), whereas for the rest of the models it was below 5.1×10^{-5}.

Next, we simulated the diffraction pattern produced by random objects and measured the execution times of each model for N varying from 10 to 512. Figure 4 shows the results, where the solid lines correspond to the proposed models, the dotted lines to the finite point sources method,

Optics EXPRESS

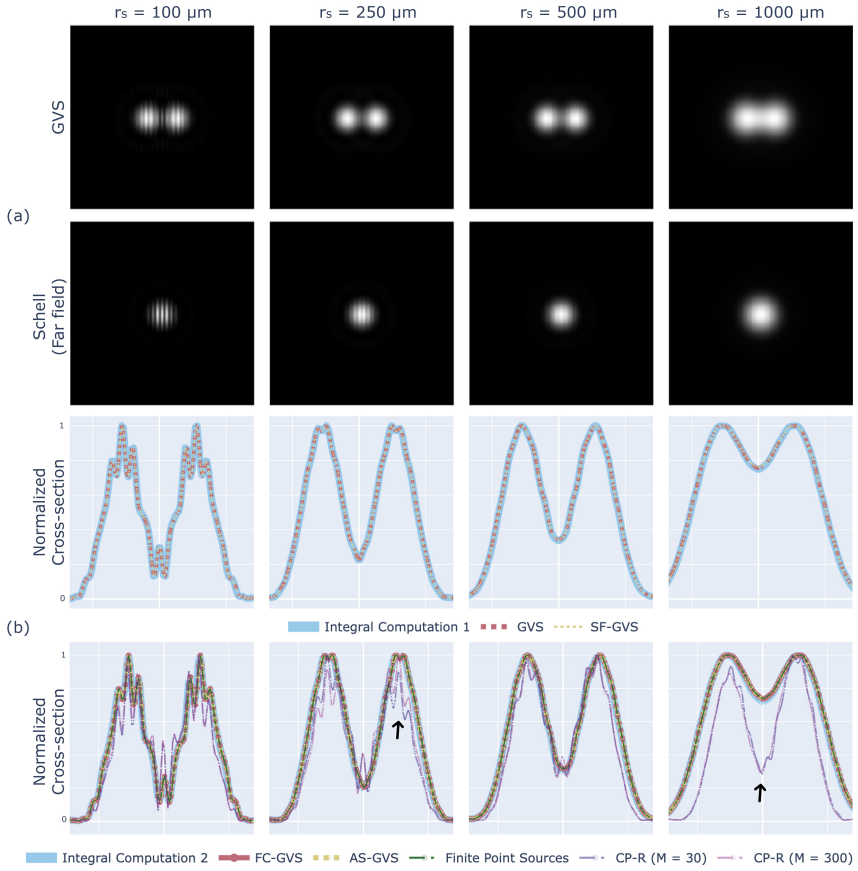

Fig. 3. Diffraction patterns produced by the double pinhole simulation at $z_{oc} = 10\ mm$; with $\lambda = 633\ nm$, $N = 256$, $z_{so} = 10\ cm$, $r_p = 25\ \mu m$, $\Delta_p = 200\ \mu m$, $\Delta x_c = 5\ \mu m$ and r_s increasing from left (high coherence) to right (low coherence); (a) 2D diffraction patterns for the GVS and far field Schell models; (b) Normalized central cross-sections for the different implemented models.

and the dotted-dashed lines correspond to CP-R. It is evident that the proposed models are several orders of magnitude faster than the ones used by other authors; their execution time is not affected by the degree of coherence of the source, and they do not suffer from the speed-accuracy trade-off. The difference in execution time from the proposed models depends mostly on the number of FFTs required. This is why the SF-GVS is slower, requiring five FFTs for its computation. We ran these experiments in the Hydra supercomputing cluster from the Vlaams Supercomputer Centrum, using an AMD EPYC 9384X processor running at 3.1 GHz and 6 GB of RAM.

One example of a random object with $N = 40$ and zero-padding is shown in Fig. 5(a), and the central cross-section of the diffraction pattern that it produces at $z_{oc} = 2\ cm$ is shown in Fig. 5(b). Figure 5(c) is a box plot of the MSE between the proposed models and the integral computation for different random objects and parameters of the simulations. The median MSE was 1.7×10^{-4} for the GVS, 1.3×10^{-4} for the SF-GVS, and 1.7×10^{-3} for the FC-GVS and the AS-GVS. These results confirm that the proposed models are also accurate for more complex objects with high spatial frequencies. Table 2 summarizes all the parameters that we tested in the simulation of random objects.

Optics EXPRESS

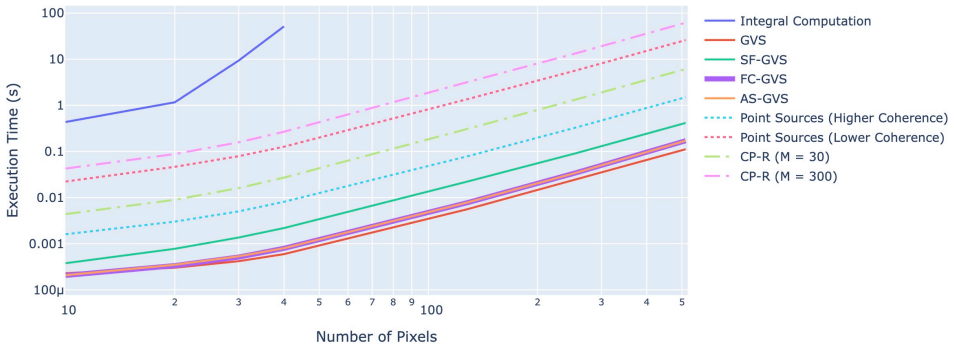

Fig. 4. Execution times for the different models as a function of N. The integral computation and our proposed models are presented in solid lines, the finite point sources method in dotted lines, and CP-R in dotted-dashed lines. Both the time and N axes are presented in a logarithmic scale.

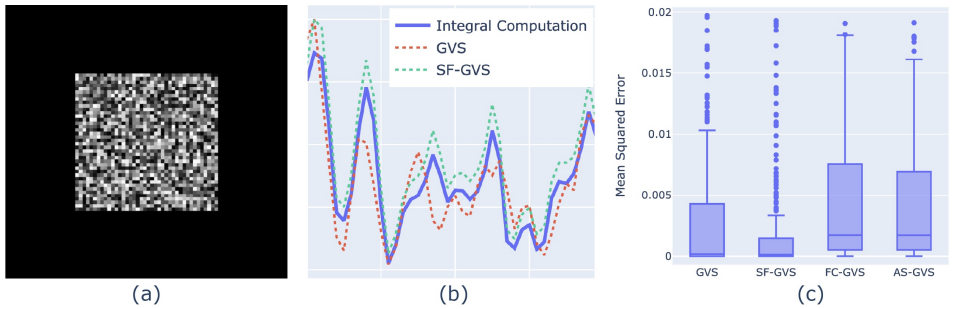

Fig. 5. Simulation with random objects; (a) example of a random object with zero-padding; (b) central cross-sections of the diffraction pattern produced by the random object in (a); (c) box plots of the MSE between the integral computation and the proposed models for all the combinations of the parameters presented in Table 2.

Table 2. Parameters tested in the simulation with random objects

λ (nm)	N	Δx_c (μm)	z_{so} (cm)	z_{oc} (cm)	r_s (μm)
633	$\{30, 40, 50, 60\}$	$\{1, 2, 5, 10\}$	10	$\{1, 2, 5, 10, 20\}$	$\{50, 100, 200, 500, 800, 1000\}$

Another important observation in this work is the fact that we can calculate the propagation of partially coherent light with arbitrary pixel pitches in the input and output planes, and we can compute off-axis propagation. These features are essential in DH and CGH applications because they allow representing different views from a 3D scene. To demonstrate this, we computed the diffraction patterns of the double pinhole experiment using the SF-GVS model for three different values of Δx_c, without changing the other parameters; and we computed the off-axis propagation of the four Cartesian quadrants to assemble a complete diffraction pattern out of four different propagations. The results are shown in Fig. 6.

Finally, we simulated the propagation of a USAF resolution target at different propagation distances using angular spectrum (coherent) and AS-GVS with three different levels of coherence. For the case of the coherent angular spectrum propagation, we accounted for the spherical illumination reaching the object plane instead of plane waves by multiplying the object matrix by

Optics EXPRESS

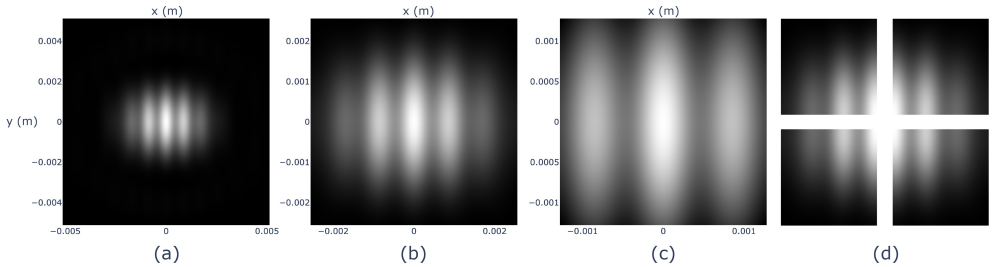

Fig. 6. Diffraction patterns produced by the double pinhole simulation with arbitrary pixel pitches and off-axis propagation using the SF-GVS model; (a) $\Delta x_c = 10\ \mu m$, (b) $\Delta x_c = 5\ \mu m$, (c) $\Delta x_c = 2.5\ \mu m$; (d) Complete diffraction pattern composed of four different off-axis propagations corresponding to the four Cartesian quadrants; with $\Delta x_c = 5\ \mu m$.

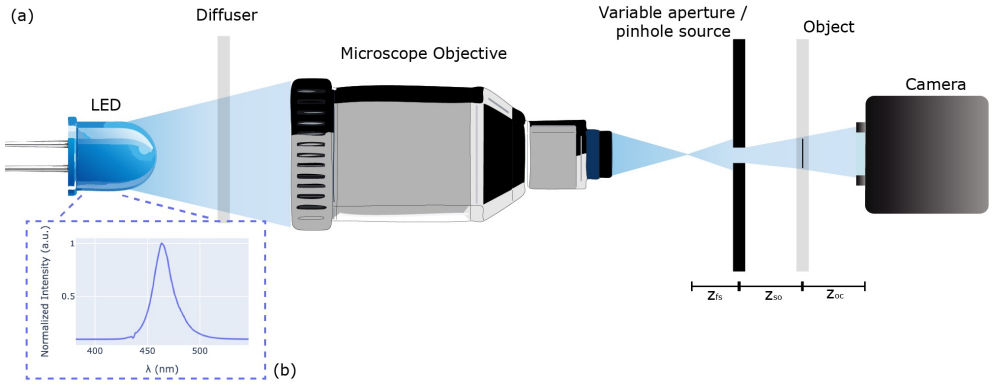

Fig. 7. (a) Optical setup used for the experimental validation; (b) Normalized emission spectrum of the blue LED used as illumination source, measured experimentally.

a spherical wave of the form e^{ikr}/r before propagating. Visualization 1 shows the continuous transition between the different propagation distances.

4. Experimental validation

To further demonstrate the validity of the proposed models, we compared them with experimental diffraction patterns obtained using partially spatially coherent illumination, i.e., LEDs. Figure 7 shows the experimental setup. Similar optical setups have been frequently applied in the field of digital lensless holographic microscopy [30,31]. To be in good agreement with the quasimonochromatic assumption, we used a blue LED as the illumination source, with 464 *nm* central wavelength and 23 *nm* full width at half-maximum. We used a 5× microscope objective to collect more light and enhance the visibility of the diffraction pattern. The diffuser was used to prevent image formation of the LED on the camera plane. We used a pinhole with a radius of 25 μm and a variable aperture ranging from 50 μm to 2 *mm* to control the degree of spatial coherence reaching the object plane. The pinhole was located at a distance $z_{so} = 3.5\ cm$ from the object plane, and the variable aperture was located at $z_{so} = 5.0\ cm$. In the experiments, we used four different objects: a double slit, a triple slit, a quadruple slit and a USAF test resolution target; and we measured the diffraction patterns at three different propagation distances (z_{oc}): 1.3 *cm*, 3.8 *cm* and 6.3 *cm*. The slits' width and spacing were 50 μm and 100 μm, respectively. In the simulations, we considered the pinhole-aperture plane to be the source plane, we set $r_s = 25\ \mu m$

Optics EXPRESS

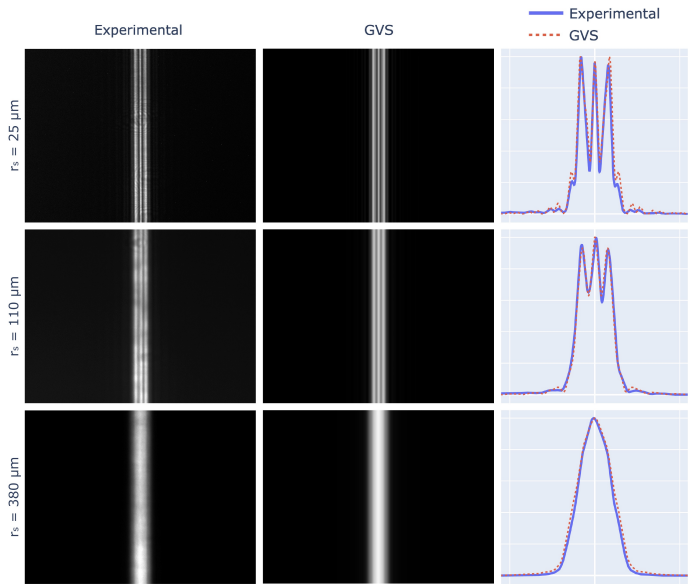

Fig. 8. Comparison between the diffraction patterns obtained experimentally and in simulation for the double slit object at $z_{oc} = 1.3\ cm$ for different values of r_s. The column on the right shows the normalized averaged cross-sections.

for the case of the pinhole, and we varied r_s from 50 μm to 2 mm in the case of the variable aperture. To capture the diffraction patterns, we used a DMK 33GX226 monochromatic camera manufactured by the Imaging Source, with 4000 × 3000 pixels and pixel pitch of 1.85 μm in both x and y directions.

We present the comparison between the experimental results and the simulations in Figs. 8 to 11. Figures 8 and 9 show the diffraction patterns and the normalized averaged cross-sections obtained by varying r_s for the double slit object at $z_{oc} = 1.3\ cm$, and the quadruple slit object at $z_{oc} = 3.8\ cm$, respectively; demonstrating excellent agreement between experiments and simulations. In Fig. 10, we present the diffraction of the triple slit object at $z_{oc} = 6.3\ cm$ and using $r_s = 190\ \mu m$ in the simulations. The distance of the spherical wave for the coherent propagation corresponds to the distance between the focal point after the microscope objective and the object plane, $z_{fo} = z_{fs} + z_{so} = 5.5\ cm$ in our case. This result shows the large error of the coherent propagation in a partially coherent scenario, highlighting the importance of properly modeling the partially coherent illumination. Finally, we performed a qualitative validation of the proposed models using a much more complex object (Fig. 11), where we show the experimental and simulated diffraction patterns produced by the USAF resolution target at $z_{so} = 1.3\ cm$ for different values of r_s. Again, the simulation results are in excellent agreement with the experiments.

Optics EXPRESS

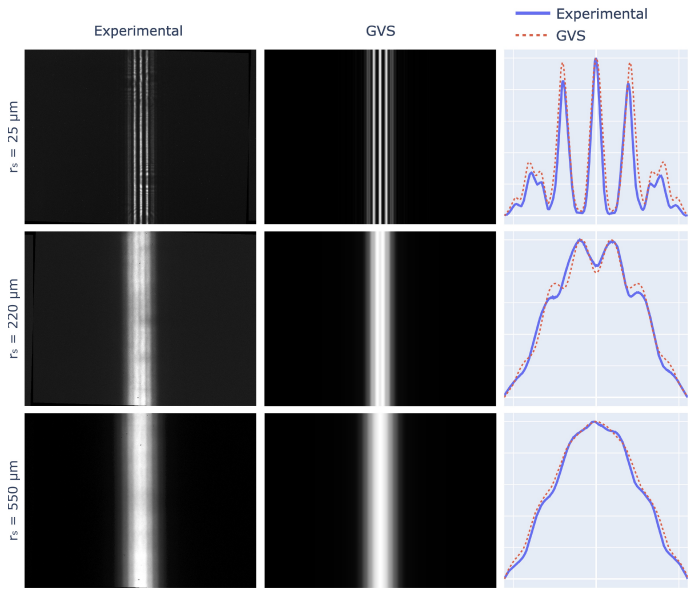

Fig. 9. Comparison between the diffraction patterns obtained experimentally and in simulation for the quadruple slit object at $z_{oc} = 3.8\ cm$ for different values of r_s. The column on the right shows the normalized averaged cross-sections.

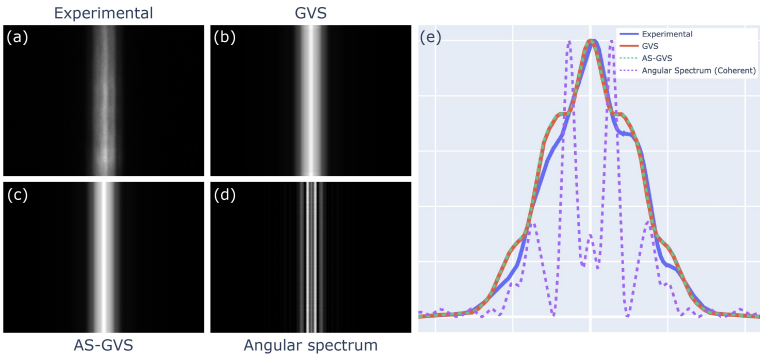

Fig. 10. Comparison between the 2D diffraction patterns obtained for the triple slit object at $z_{oc} = 6.3\ cm$ and using $r_s = 190\ \mu m$ in the simulations (a-d). The normalized averaged cross-sections are presented in (e).

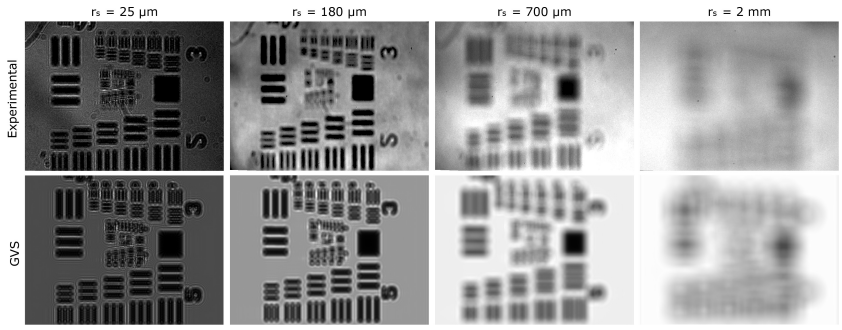

Fig. 11. Comparison between the diffraction patterns obtained experimentally and in simulation for the USAF resolution target at $z_{oc} = 1.3\ cm$ for different values of r_s.

Optics EXPRESS

5. Conclusion

In this work, we introduced the GVS propagator, an algorithm that can efficiently model the propagation of partially spatially coherent light, based on the Van Cittert-Zernike and the generalized Schell's theorems. The algorithm is computed using multiple FFTs, it uses only the Fresnel and paraxial approximations, and it only requires one single forward propagation, making it highly accurate and orders of magnitude faster than other methods that are currently used in computational imaging. We provided the mathematical derivation of the model, the way to compute it numerically in terms of Fourier transform operations, and the way to compute it using any existing coherent propagator. We implemented multiple variations of the algorithm using different coherent propagators and demonstrated their accuracy by performing a series of numerical experiments. The proposed models are well-suited for modeling near-field diffraction, in contrast to the traditional Schell's theorem. We showed this fact by simulating the diffraction at short distances of a double pinhole illuminated with different levels of spatial coherence. Using this same simulation, we also demonstrated that the proposed models are more accurate than CP-R, which suffers from the speed-accuracy trade-off. Furthermore, we confirmed that our framework is also valid when treating the diffraction of more complex objects containing high spatial frequencies, such as random objects, by comparing it with the discrete integral computation. One of the highlights of our work is the great computational efficiency achieved with the GVS method and its variants. We presented a comparison of the execution time from our models, the state-of-the-art, and the integral computation for different values of N, showing that our models are several orders of magnitude faster and their execution time is not dependent on the degree of coherence of the light source. In addition, we illustrated the diffraction of partially coherent light with arbitrary pixel pitches and off-axis propagation using the SF-GVS propagator, showcasing the flexibility of the proposed framework and its great potential for DH and CGH applications. Finally, we performed a series of optical experiments where we varied the radius of the light source, the diffracting object, and the propagation distances; further validating the accuracy and efficiency of the proposed framework with large grids (4000×3000 pixels). We tested objects containing a different number of slits and a USAF resolution target, finding an excellent agreement between the simulations and the experiments. Further research efforts will center on efficient algorithms to model spatio-temporal coherence, and other efforts will focus on applications of the proposed algorithms in CGH and DH. After this work, we can do efficient simulations with partial spatial coherence, and the propagation algorithm can be seamlessly integrated into implementations that currently rely on the traditional coherent propagators. Therefore, we believe that this work can benefit many fields within computational imaging.

Funding. Fonds Wetenschappelijk Onderzoek (12ZQ223N, G089424N, G0A3O24N, 11PGG24N).

Disclosures. The authors declare no conflicts of interest.

Data Availability. Experimental data may be obtained from the authors upon reasonable request. For simulations, see [29].

References

1. J. W. Goodman, *Introduction to Fourier optics* (W.H. Freeman, Macmillan Learning, 2017), 4th ed.
2. J. W. Goodman, *Statistical Optics* (Wiley, 2015), 2nd ed.
3. L. Raimondi and D. Spiga, "Mirrors for X-ray telescopes: Fresnel diffraction-based computation of point spread functions from metrology," Astronomy Astrophysics **573**, A22 (2015).
4. X. Weng and L. T. Vuong, "Fractal, diffraction-encoded space-division multiplexing for FSO with misalignment-robust, roaming transceivers," Sci. Rep. **12**(1), 2777 (2022).
5. E. M. Ali, M. Alibakhshikenari, N. A. Elmunim, *et al.*, "Defected ground structure antenna array with metasurface inspired interlinked CSRR for 5G millimeter wave applications," Sci. Rep. **15**(1), 1–14 (2025).
6. R. Leitgeb, A. F. Fercher, and C. K. Hitzenberger, "Performance of fourier domain vs. time domain optical coherence tomography," Opt. Express **11**(8), 889–894 (2003).

Optics EXPRESS

7. C. J. Mann, L. Yu, C.-M. Lo, *et al.*, "High-resolution quantitative phase-contrast microscopy by digital holography," Opt. Express **13**(22), 8693–8698 (2005).
8. J. Rosen, S. Alford, B. Allan, *et al.*, "Roadmap on computational methods in optical imaging and holography [invited]," Appl. Phys. B **130**(9), 166 (2024).
9. T. Shimobaba, J. Weng, T. Sakurai, *et al.*, "Computational wave optics library for C++: CWO++ library," Comput. Phys. Commun. **183**(5), 1124–1138 (2012).
10. M. Testorf, B. Hennelly, and J. Ojeda-Castañeda, *Phase-Space Optics: Fundamentals and Applications* (McGraw-Hill Education, New York, 2010), 1st ed.
11. L. Waller, G. Situ, and J. W. Fleischer, "Phase-space measurement and coherence synthesis of optical beams," Nat. Photonics **6**(7), 474–479 (2012).
12. J. J. Rogers, T. Kirk, P. Di Pasquale, *et al.*, "Phase-Space propagator for partially coherent wave fields in the spatial domain," Opt. Commun. **587**, 131814 (2025).
13. E. Wolf, "New theory of partial coherence in the space-frequency domain. Part I: spectra and cross spectra of steady-state sources," J. Opt. Soc. Am. **72**(3), 343–351 (1982).
14. G. Gbur, "Partially coherent beam propagation in atmospheric turbulence [Invited]," J. Opt. Soc. Am. A **31**(9), 2038–2045 (2014).
15. P. Vahimaa, J. Turunen, L. Mandel, *et al.*, "Finite-elementary-source model for partially coherent radiation," Opt. Express **14**(4), 1376–1381 (2006).
16. Y. Kawata, S. Watanabe, Y. Suzuki, *et al.*, "Numerical simulations of partially coherent illumination for multi-scattering phase objects via a beam propagation method," Appl. Opt. **58**(4), 954–962 (2019).
17. T. Nobukawa, N. Ishii, T. Muroi, *et al.*, "Incoherent digital holography simulation based on scalar diffraction theory," J. Opt. Soc. Am. A **38**(7), 924–932 (2021).
18. N. Chauvet, T. Aoki, A. Röhm, *et al.*, "Compressive propagation with coherence," Opt. Lett. **47**(3), 613–616 (2022).
19. R. Suda, R. Horisaki, and M. Naruse, "Incoherent computer-generated holography," Opt. Lett. **47**(15), 3844–3847 (2022).
20. R. Horisaki, O. Shigematsu, and M. Naruse, "Computer-generated holography with ordinary display," Opt. Lett. **49**(8), 1876–1879 (2024).
21. K. A. Nugent, "A generalization of Schell's theorem," Opt. Commun. **79**(5), 267–269 (1990).
22. M. J. Lopera, C. Buitrago-Duque, J. Garcia-Sucerquia, *et al.*, "Simulation of digital lensless holographic microscopy holograms: a physics-image processing approach," Opt. Express **32**(27), 48509–48524 (2024).
23. A. C. Schell, "A Technique for the Determination of the Radiation Pattern of a Partially Coherent Aperture," IEEE Trans. Antennas Propag. **15**(1), 187–188 (1967).
24. J. Zhong, L. Tian, P. Varma, *et al.*, "Nonlinear Optimization Algorithm for Partially Coherent Phase Retrieval and Source Recovery," IEEE Trans. Comput. Imaging **2**(3), 310–322 (2016).
25. Z. Zhao, J. Duan, and J. Liu, "Speckle reduction in holographic display with partially spatial coherent illumination," Opt. Commun. **507**, 127604 (2022).
26. F. Wang and O. Korotkova, "Convolution approach for beam propagation in random media," Opt. Lett. **41**(7), 1546–1549 (2016).
27. Y. Zhu, Z. Dong, F. Wang, *et al.*, "Compact generation of robust Airy beam pattern with spatial coherence engineering," Opt. Lett. **47**(11), 2846–2849 (2022).
28. D. G. Voelz and M. C. Roggemann, "Digital simulation of scalar optical diffraction: revisiting chirp function sampling criteria and consequences," Appl. Opt. **48**(32), 6132–6142 (2009).
29. M. Montoya, "Partially Coherent Propagator in Python," https://github.com/mmonto952/gvs-propagator (2025).
30. J. Garcia-Sucerquia, W. Xu, S. K. Jericho, *et al.*, "Digital in-line holographic microscopy," Appl. Opt. **45**(5), 836–850 (2006).
31. M. J. Lopera and C. Trujillo, "Holographic point source for digital lensless holographic microscopy," Opt. Lett. **47**(11), 2862–2865 (2022).